Journal of Alloys and Compounds 769 (2018) 420–429

Contents lists available at ScienceDirect

Journal of Alloys and Compounds

journal homepage: http://www.elsevier.com/locate/jalcom

White light emission from single-phase Y_2MoO_6: xPr^{3+} (x = 1, 2, 3 and 4 mol%) phosphor

L.X. Lovisa [a, *], A.A.G. Santiago [a], M.B. Farias [a], B.S. Barros [b], E. Longo [c], M.S. Li [d], C.A. Paskocimas [a], M.R.D. Bomio [a], F.V. Motta [a]

[a] LSQM—Laboratório de síntese química de materiais - DEMAT, UFRN, Campus Lagoa Nova, CEP 59078-900, Natal, RN, Brazil
[b] Universidade Federal de Pernambuco, Departamento de Engenharia Mecânica, Av. Prof. Moraes Rego-1235, Cidade Universitária, Recife, PE, Brazil
[c] LIEC—Laboratório interdisciplinar de eletroquímica e cerâmica, UFSCar, São Carlos Rua Francisco Degni s/n, CEP 14801-907 Araraquara, SP, Brazil
[d] IFSC—Instituto de Física de São Carlos, USP, São Paulo, Av. Trabalhador São-carlense, Centro, CEP 13566-590, São Carlos, SP, Brazil

ARTICLE INFO

Article history:
Received 29 April 2018
Received in revised form
28 July 2018
Accepted 30 July 2018
Available online 2 August 2018

Keywords:
Photoluminescence
Y_2MoO_6: x%Pr^{3+}
White light emitting

ABSTRACT

A series of Pr^{3+} doped with Y_2MoO_6 was synthesized using the co-precipitation method and the structural, photoluminescent and morphological properties of XRD, scanning electron microscopy (SEM) and photoluminescence spectrometry were investigated. The most intense absorption of its host matrix occurred between 200 and 340 nm due to a charge transfer in O → Mo. The photoluminescence emission results of Y_2MoO_6: x%Pr^{3+}particles showed some white emission due to a strong contribution of the matrix and the Pr^{3+}dopant. All samples exhibited high color rendering index (>90%), indicating that the light source can reproduce colors. It was possible to obtain a white-emitting single-phase luminescent material from an easy route of production. The investigation indicated that Y_2MoO_6: x%Pr^{3+} is a potential candidate for applications with white light emitting diodes.

1. Introduction

Constant efforts have been made in the research of new luminescent materials to be used in optical devices. This group of materials emerges as a very promising class of new solid state light sources for application in lighting and display devices [1–5]. Luminescent materials correspond to an order of materials that have aroused a growing industrial interest due to their wide range of applications such as WLEDs (white light emitting diodes), FEDs (field emission displays) and CRTs (cathode ray tubes) [6–8]. As a result, in the scientific environment, the aim is to obtain materials that meet the current market expectations in order to produce stable materials with high efficiency and reproducibility.

The first approach for WLED production was the combination of materials: YAG: Ce^{3+} (issued in yellow) with InGaN (issued in blue) [9], these phosphors became the most commercial and popular materials. However, yellow phosphors show some limitations such as low color rendering index (CRI) and low color temperature stability. In addition, the illumination color of this device is quite sensitive to changes in transmission voltage and, therefore, stable WLEDs are difficult to produce [10].

WLEDs arise by combining excited **r**ed-**g**reen-**b**lue (**RGB**) and phosphors in the ultraviolet region to optimize the color yield properties [11]. WLEDs with multiple emitting components may be questionable because the color balance is difficult to control. In this situation, single-phase phosphorus, which emerges as white emitters, presents luminous efficiency, excellent CRI, adjustable temperature and purity in its chromaticity coordinates [12].

Naresh et al. [13] used zinc borate matrix combined with Tm^{3+}, Tb^{3+} and Eu^{3+} ions under ultraviolet light excitation to generate white light emission, obtaining satisfactory results regarding purity, reproducibility and proximity properties of the standard white light conditions. Their study was based on the evaluation of energy transfers among doping elements. Yang et al. [14] produced Sr_3Y-$Na(PO_4)_3F$: Dy^{3+} from solid state reaction and studied the thermal and chemical stability of the compound for photoluminescent use. It was verified that the high activation energy results in good thermal stability and that doping with the Dy^{3+} promoted simultaneous emitters in the violet (326–390 nm), blue (483 nm) and yellow regions (580 nm), allowing emitting white phosphor for white LEDs.

Grzyb et al. [15] studied the modification of color and time of life

* Corresponding author.
E-mail address: lauraengmat@hotmail.com (L.X. Lovisa).

https://doi.org/10.1016/j.jallcom.2018.07.339
0925-8388/

decay from the variation of the dopant concentration used in Sr_2CeO_4. The introduction of lanthanide ions (Dy^{3+} and Eu^{3+}) into the Sr_2CeO_4 structure turned the color of the matrix emission. The color emission can easily be adjusted by changing the dopant concentration.

Based on the results obtained by single-phase phosphors [16,17], researchers developed numerous surveys about the production of white emitters using single host matrix. Shang et al. [18] mentioned four possible methods to obtain white light in single-phase dies: (i) emission in white can be generated from the doping of only one type of rare earth in the matrix [14]; (ii) white light can be generated by combining multiple rare earth ions with simultaneous different emissions: red, green and blue; yellow and blue (such as $Ho^{3+}/Yb^{3+}/Tm^{3+}$, $Tm^{3+}/Tb^{3+}/Eu^{3+}$) [19,20]; (iii) the emission of white light can be generated by the association of ions in pairs based on the energy transfer mechanism (Eu^{3+}/Tb^{3+}, Tm^{3+}/Er^{3+}, Tm^{3+}/Ho^{3+}, Dy^{3+}/Eu^{3+}, Dy^{3+}/Sm^{3+}) [21–27] and (iv) luminescent materials related to electronic defects may also emit white light [28].

Metallic molybdates ($AMoO_4$ and/or A_2MoO_6, A = metal cation) are considered good hosts for luminescent materials due to their excellent chemical stability [29–32]. Another important feature is their extensive and intense ultraviolet charge transfer absorption bands, which make them good energy receptors [33]. The class of molybdates has attracted interest in numerous scientific and technological fields due to the innumerous industrial applications, including scintillation detectors, optical fibers, moisture sensors, solid state lasers, catalysts and photoluminescent devices [34–36]. Studies have been intensified to obtain new functionalities and behaviors in relation to their wide range of properties and applications [37].

The crystalline structure of Y_2MoO_6 was detailed by Alonso et al. [38]. According to the authors, Y atoms occupy three non-equivalent crystallographic sites and are coordinated by eight O atoms. Mo atoms are coordinated to five O atoms, four of which, at short distance and the last one at long distance. Y_2MoO_6 is an excellent matrix for trivalent rare earth doped due to its physical and chemical properties [39,40].

The trivalent praseodymium ion (Pr^{3+}) has configuration of energy levels represented by spectral emission lines in UV, visible and infrared range. In recent years, various materials have been extensively investigated in relation to their various potential applications, such as fiber laser amplifier [41], red-emitting phosphors [42,43] and laser up-conversion [44]. Pr^{3+} ion presents the following specific ^3P_J transitions (J = 0, 1, 2) approximately located at 478, 459 and 428 nm, respectively [45].

In this sense, this study aimed to investigate the photoluminescent properties of Y_2MoO_6: x%Pr^{3+}capable of emitting white light. Y_2MoO_6: x%Pr^{3+} particles were characterized by the following techniques: X-Ray Diffraction, Uv–Visible Absorption Spectroscopy, Photoluminescence and Scanning Electron Microscopy.

2. Experimental

2.1. Materials

Sodium molybdate dihydrate ($Na_2MoO_4{\cdot}2H_2O$), (Alfa Aesar), Yttrium Nitrate Hexahydrate ($Y(NO_3)_3{\cdot}6H_2O$) (Alfa Aesar), Praseodymium(III) nitrate ($Pr(NO_3)_3.xH_2O$) (Alfa Aesar), Ammonium hydroxide (NH_4OH) (Synth) and distilled water were used as soon as they were received to prepare Y_2MoO_6 and Y_2MoO_6: x% Pr^{3+}particles.

2.2. Experimental procedures

Two precursor solutions were prepared for the synthesis of Y_2MoO_6: x%Pr^{3+} particles: one containing molybdenum (solution **A**) and the other containing yttrium (solution **B**). For both solutions, the starting reagent was dissolved in 40 ml of distilled water. After dissolution, solution **B** was added to solution **A** dropwise. After its complete dissolution, the dopant (Pr^{3+}) was added to the system. Finally, NH_4OH was added to the solution to stabilize its pH at 8. The solution was centrifuged three times in distilled water and then left to dry in oven at temperature of 80 °C for 24 h. Particles were calcined at 1000 °C for 2 h at heating rate of 10 °C/min. Pr^{3+} concentration varied from 1, 2, 3 and 4 mol%.

2.3. Characterization of Y_2MoO_6: x%Pr^{3+}particles

Y_2MoO_6: x%Pr^{3+} particles were structurally characterized by XRD using Shimadzu XRD 7000 instrument with Cu-Kα radiation (λ = 1.5406 Å) in the 2θ range from 10 to 80° at scanning rate of 0.02° s^{-1}. Lattice parameters and position were determined by means of the Rietveld refinement method [46] and were analyzed by the Structure Analysis System (GSAS) software with EXPGUI graphical interface software [47]. The lattice parameters and atomic positions obtained were used to model these unit cells using the Visualization for Electronic and Structural Analysis (VESTA) software [48], version 3.1.2. The morphologies and the dispersion of the atoms of samples were investigated by EDS spectroscopy using field-emission gun scanning electron microscopy (FEG-SEM; Carl Zeiss, Supra 35-VP Model, Germany) operated at 14 kV. The Uv–visible reflectance spectra of powders were performed using Shimadzu spectrophotometer, model UV-2600. The Photoluminescence (PL) spectra were acquired with Ash 27 monochromator Monospec (Thermal Jarrel, U.S.A.) and R4446 photomultiplier (Hamamatsu Photonics, U.S.A.). The 350 nm beam of a krypton ion laser (Coherent Innova 90 K) was used as the excitation source while its maximum output power was kept at 200 mW. All measurements were performed at room temperature. Uv–Vis and PL spectra were performed three times for each sample to ensure reliability of measurements.

3. Results and discussion

3.1. X-Ray Diffraction of Y_2MoO_6: x%Pr^{3+}

From XRD analysis, it was possible to identify that all diffraction peaks presented in Fig. 1 are indexed according to reference JCPDS 52–650, which represents the monoclinic crystal structure. No additional peaks of secondary phases are observed. It is reasonable to consider that Y^{3+} ions were successfully replaced by Pr^{3+} ions. The exchange of ions was favored because cations presented very similar characteristics: (i) approximate ionic radii: Y^{3+} (0.90 Å) and Pr^{3+} (1.00 Å) and (ii) have the same valence. A peak (221) displacement (θ ≈ 29°) was observed for the lowest angle region in the inset of Fig. 1 as the Pr^{3+} concentration increased. This behavior is explained by the disorder caused due to the $Y^{3+} \rightarrow Pr^{3+}$ replacement, since the incorporation of Pr^{3+} ions into the Y_2MoO_6 lattice induces local distortion in the crystal structure. The same behavior was verified in another work that used Y_2MoO_6 as its host matrix [49]. The unit cell may undergo changes in its volume, contraction or expansion as its chemical composition changes.

The crystallite size and the microdeformation in the lattice are two properties that can be studied from the analysis of the half height of the diffraction peak (FWMH) and its intensity. Microdeformation can occur in several ways such as: contact or sinter stress, grain boundary, triple junction, stacking faults and

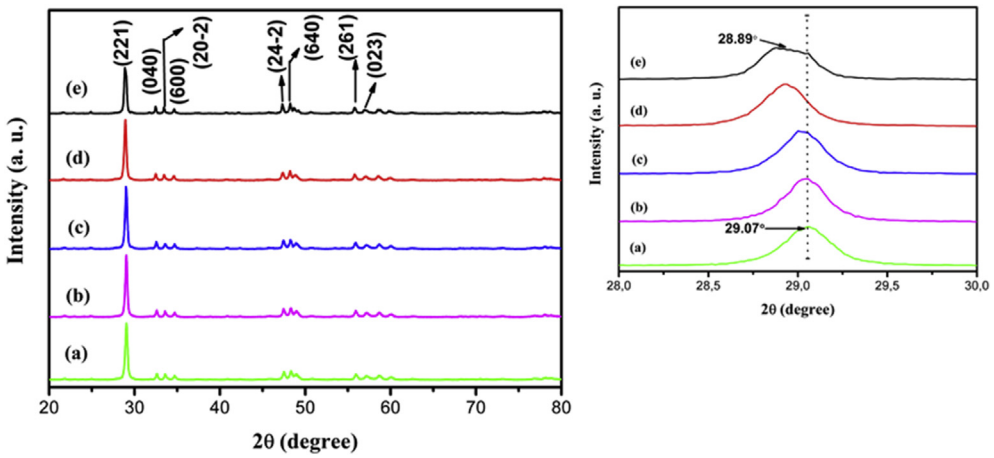

Fig. 1. XRD patterns of Y_2MoO_6: x%Pr^{3+} (a = 0, b = 1, c = 2, d = 3 and e = 4 mol) particles.

coherency stress [50]. The mean crystallite size was estimated by the Scherrer equation (1).

$$D = \frac{0.9\lambda}{\beta Cos\theta} \quad (1)$$

Where D is the mean crystallite size, λ is the wavelength, θ is half the Bragg angle and β is the half height of the selected reflection (FWHM). For the D calculation, the average value of peaks (221), (040), (20-2), (600), (24-2), (640), (261), (023) was considered. Table 1 shows the crystallite size values, the microdeformation and the position of the diffraction peak in the plane (221).

Based on the XRD results, refinement was performed using the GSAS software Fig. 2 presents the results of Rietveld refinements, observing that the differences between experimentally observed diffraction patterns and theoretically calculated data (Obs-Calc line) are close to zero, showing that the diffraction patterns of samples are well adapted. The crystallographic and refinement quality parameters are recorded in Table 2; more details are provided in the Support Information (Table S1). The reliability parameters χ^2, R_{wp} and R_p indicate good quality of structural refinements and numerical results.

Y_2MoO_6 crystallizes into a monoclinic structure with $C_{2/c}$ space group. The lattice parameters and unit cell volume of samples are in agreement with literature. Hou et al. [51] synthesized Y_2MoO_6 using the solid state reaction and the lattice parameter values obtained were a = 16.3504 Å, b = 11.0192 Å, c = 5.3486 Å, β = 108.49° and unit cell volume equal to 913.86 $Å^3$. Note that the unit cell volume of samples (Table 2) slightly increases with the replacement of Y^{3+} ions by Pr^{3+} ions, this is because Pr^{3+} ions present a slightly higher ionic radius than Y^{3+}ions (1.00 Å and 0.90 Å, respectively), thus causing expansion and distortion in the lattice. According to the positions of Y, Mo and O atoms obtained by the structural analysis, the crystalline structures of samples Y_2MoO_6: x %Pr^{3+} (Pr = 0, 1, 2, 3 and 4 mol) were plotted with the aid of the VESTA software as shown in Fig. 3. MoO_5 clusters are highlighted. Y_2MoO_6 crystallizes in the $C_{2/c}$ space group, with 8 formula units in the unit cell. "The structure contains four zigzags, one-dimensional MoO_5 polyhedral row per unit cell, running through the RO_8 polyhedral framework along the [001] direction. MoO_5 form discrete units (i.e. do not share common oxygen), with Mo–O distances ranging from 1.77 to 2.24 Å, although the oxygen coordination can be extended to distances of about 3.1 Å, giving rise to strongly distorted MoO_8 scale. Thus, MoO_8 and RO_8 polyhedral are fully ordered in R_2MoO_6 compounds, which, in fact, can be considered as fluorite superstructures (M_3O_6), containing 24 MO_2 fluorite units per unit cell" [39]. Changes are observed in the distances between Mo–O bonds; these changes occur due to distortions caused in the Y_2MoO_6 lattice introduced by the effect of Pr^{3+} doping and the tensions generated by the synthesis conditions that were applied. The values of Mo–O distances are in agreement with literature, Alonso et al. [38] analyzed the structure of Y_2MoO_6 and obtained the distances of Mo–O bonds (Mo–O1 = 1.788 Å, Mo–O2 = 1.786 Å, Mo–O3 = 1.808 Å, Mo–O4 = 1.804 Å and Mo–O5 = 2.215 Å), and the MoO_5 polyhedral was formed by four short Mo–O bonds and one long Mo–O bond.

3.2. Uv–Vis absorbance spectra of Y_2MoO_6: x%Pr^{3+}

Fig. 4 shows the Uv–Vis absorbance spectra of Y_2MoO_6 and Y_2MoO_6: x%Pr^{3+}. A high absorption band is observed up to 340 nm. This absorption band occurs mainly due to the absorption of the charge transfer (CT) within $[MoO_4]^{2-}$ clusters [52]. It was verified that the presence of Pr^{3+} causes an increase in the absorption band for the green/yellow region in relation to the undoped sample, as well as the existence of a discrete band referring to the $^3H_4 \rightarrow {}^3P_0$ transition at 493 nm characteristic of Pr^{3+}.

The optical band gap of undoped, 1, 2, 3 and 4 mol% Pr^{3+}

Table 1
Values of strain, crystallite size, FWHM (221) and Height of the plane (221) of Y_2MoO_6: x % Pr (Pr = 0, 1, 2, 3 and 4 mol %) particles.

Samples	Strain (ε)	Crystallite size (nm)	Position of the diffraction peak (221)
		Scherrer's formula	
Y_2MoO_6	1.0978×10^{-4}	22.68	29.07°
Y_2MoO_6:1%Pr	8.0910×10^{-4}	30.57	29.02°
Y_2MoO_6:2%Pr	$1{,}1640 \times 10^{-3}$	21.45	29.01°
Y_2MoO_6:3%Pr	1.1240×10^{-3}	22.21	28.92°
Y_2MoO_6:4%Pr	1.1030×10^{-3}	22.63	28.89°

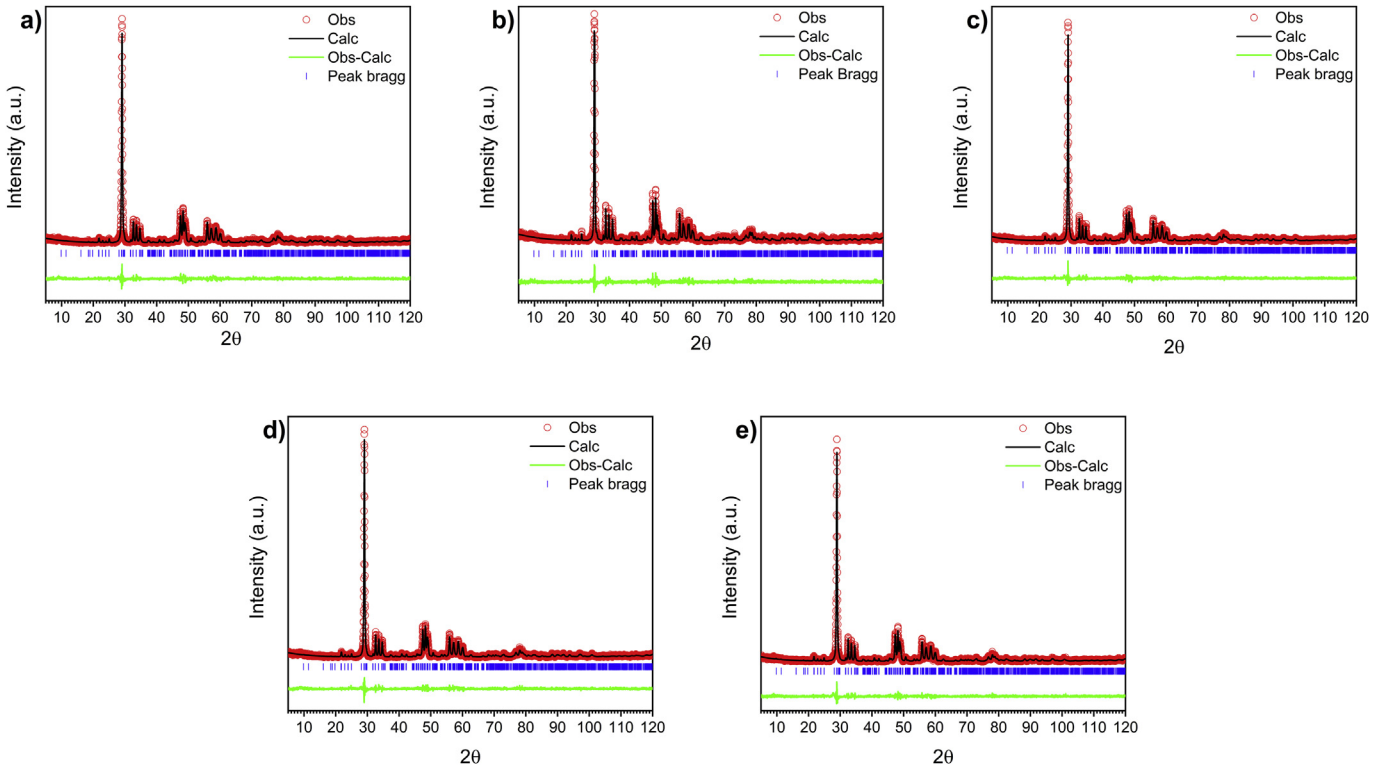

Fig. 2. Rietveld refinement of Y_2MoO_6: x%Pr^{3+} (a = 0, b = 1, c = 2, d = 3 and e = 4 mol) particles.

Table 2
Parameters of the Rietveld refinement of the particles Y_2MoO_6: x% Pr (x = 0, 1, 2, 3 and 4 mol %).

Samples	Y_2MoO_6	Y_2MoO_6:1%Pr	Y_2MoO_6:2%Pr	Y_2MoO_6:3%Pr	Y_2MoO_6:4%Pr	Ref [JCPDS 52–650]
Crystal system	Monoclinic	Monoclinic	Monoclinic	Monoclinic	Monoclinic	Monoclinic
Space Group	$C_{2/c}$	$C_{2/c}$	$C_{2/c}$	$C_{2/c}$	$C_{2/c}$	$C_{2/c}$
Lattice parameters (Å)						
a	16.4122	16.3826	16.4134	16.4213	16.4173	16.3538
b	11.0089	11.0227	11.0180	11.0152	11.0178	11.0183
c	5.3468	5.3531	5.3447	5.3472	5.3499	5.3506
β (°)	108.66	108.57	108.69	108.71	108.69	108.52
α = *γ* (°)	90	90	90	90	90	90
V(Å)^3	915.25	916.9	915.56	916.10	916.68	914.18
X^2	1.35	1.44	1.43	1.45	1.39	
Rwp (%)	17.59	18.76	17.80	18.04	17.60	
Rb (%)	12.78	14.02	13.00	13.10	13.90	

materials was evaluated from the absorption spectra. The absorption spectra *F*(*R*) were calculated from the reflection spectra using the Kubelka-Munk function [53]:

$$F(R) = \frac{(1-R)^2}{2R} = \frac{K}{S} \quad (2)$$

where *R* is the reflectance, *K* is the absorption coefficient, and *S* is the scattering coefficient. The bandgap value of Y_2MoO_6 and Y_2MoO_6: x%Pr^{3+} was evaluated by extrapolating the linear portion of the curve. The gap energy obtained for samples is between 3.41 and 3.46 eV.

3.3. Photoluminescence properties of Y_2MoO_6: x%Pr^{3+}

Fig. 5 (a) shows the photoluminescent emission spectra of Y_2MoO_6 and Y_2MoO_6: x%Pr^{3+}particles. Samples were excited by a wavelength laser (λ) of 350 nm at room temperature. The presence of three broad bands centered at 440, 545 and 620 nm is observed in the spectrum of the pure sample in Fig. 5 (b). These bands are due to the electronic transitions in $[MoO_4]^{2-}$ clusters [51,54,55]. According to Sczancoski et al. [56], the position that the electronic defects (h) occupy in the band gap can define different types of emissions. The energy states in molybdates are formed by the oxygen 2p orbital located just above the valence band (VB) and by the molybdenum orbital 4d located under the conduction band (CB). From the deconvolution of Y_2MoO_6, it is possible to estimate how each visible region contributes to the behavior in the whole. Mo (4d) → O (2pσ) type transitions are associated to defects near the valence band, which corresponds to emissions in blue (21%). Mo (4d) → O (2pπ) type transitions are associated with distances far from the valence band [56], which correspond to emissions in green (33%) and red (46%).

PL emission is closely related to the crystal structure and distortions in the metal-oxygen polyhedra of molybdates. The distortion present in the Y_2MoO_6 structure is justified by the substitution

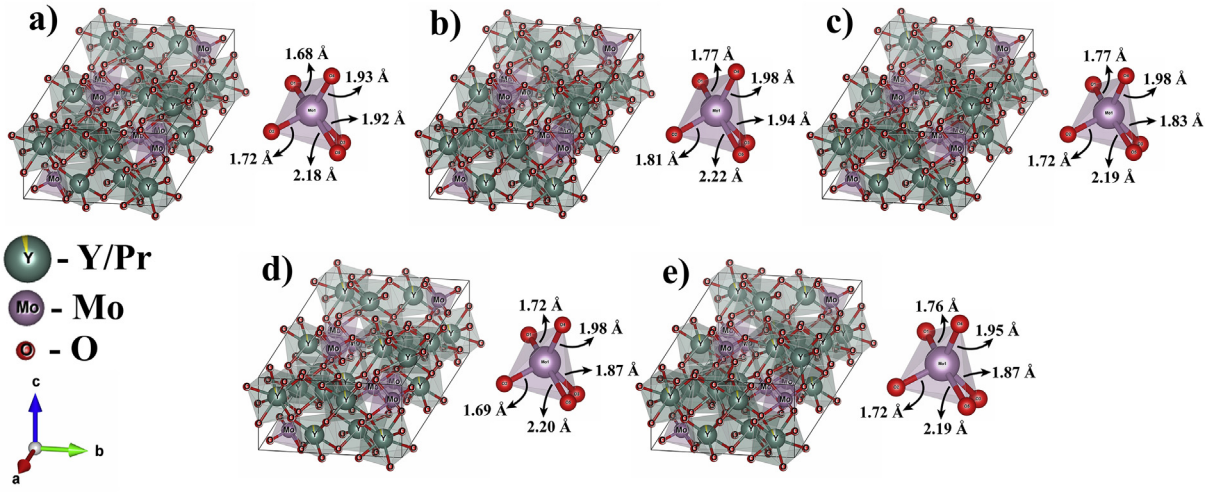

Fig. 3. Representation of the crystalline structure of Y_2MoO_6: x%Pr^{3+}(a = 0, b = 1, c = 2, d = 3 and e = 4 mol) particles.

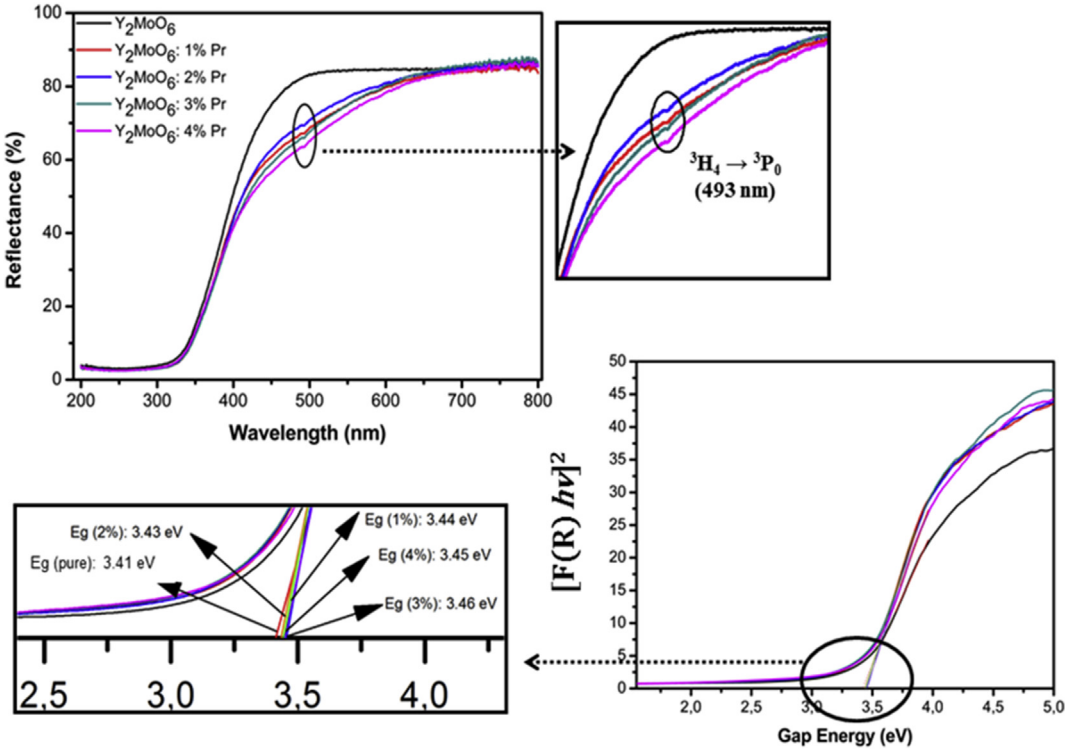

Fig. 4. UV–Vis absorbance spectra of Y_2MoO_6 and Y_2MoO_6: x%Pr^{3+} and gap energy determination.

of Y atoms for Pr. This exchange is responsible for one of the crucial components that lead to the formation of structural defects in the crystalline lattice of the matrix, that is, oxygen vacancies [57]. These oxygen vacancies were reported to be an important factor in obtaining luminescent materials that exhibit long-acting phosphorescence [58,59]. Oxygen vacancies act as centers of electron trapping. They capture electrons and gradually release them to the luminescent centers [60] and in the electron-hole recombination, luminescence with long response is observed in Refs. [61,62]. These factors probably result in a distortion process on [MoO_5] and [YO_8] (or [PrO_8]) clusters, favoring the formation of intermediate energy levels within the band gap of this material. These energy levels are composed of oxygen 2p states (near the valence band) and praseodymium 5d levels (below the conduction band). During the excitation process with 350 nm wavelength, some electrons are promoted from the oxygen 2p states to praseodymium 5d levels through the absorption of photons (hν). This mechanism results in the formation of self-trapped excitons (STEs), i.e., trapping of electrons (e^-) by holes (h). The emission process of photons (hν) occurs when an electron localized in a praseodymium 5d levels decays into an empty oxygen 2p state. Consequently, this mechanism is responsible for the PL emission of Y_2MoO_6 nanoparticles. The proposed mechanism is based on the distortion [MoO_5] and [YO_8] (or [PrO_8]) clusters.

For the Y_2MoO_6: x%Pr^{3+} series (x = 1, 2, 3 and 4 mol), the presence of f → f characteristic transitions of Pr^{3+} was observed.

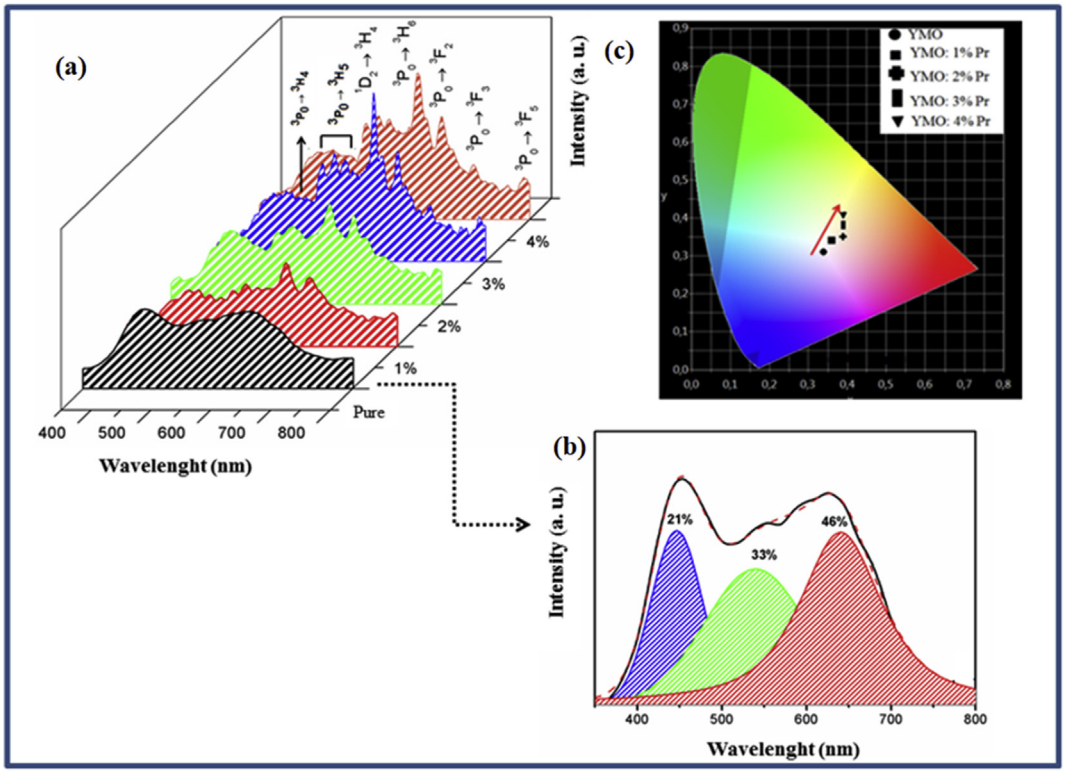

Fig. 5. (a) Emission spectra of Y_2MoO_6: x%Pr^{3+} (x = 0, 1, 2, 3 and 4 mol); (b) deconvolution curve of Y_2MoO_6 and (c) chromaticity diagram.

Pr^{3+} emission in the emission spectrum of PL in Fig. 5(a) is: $^3P_0 \rightarrow {}^3H_4$, $^3P_0 \rightarrow {}^3H_5$, $^1D_2 \rightarrow {}^3H_4$, $^3P_0 \rightarrow {}^3H_6$, $^3P_0 \rightarrow {}^3F_2$, $^3P_0 \rightarrow {}^3F_3$ and $^3P_0 \rightarrow {}^3F_5$, respectively located in, 491, 531–567, 612, 629, 654, 706 and 790 nm [63,64]. It was observed that with the addition of Pr^{3+}, the photoluminescence intensity is favored. However, for sample doped with 4 mol% Pr^{3+}, there is a drop in photoluminescence. This behavior can be justified due to a critical concentration of the dopant in the matrix lattice, known as quenching concentration. What actually occurs in this case is that Pr^{3+} ions are at a very close distance, and in this condition, the appearance of non-radioactive transitions occurs more effectively [65]. Non-radioactive transitions are expressed in phonon forms, which result in vibrations within the crystal lattice. The concentration of dopants determines the average distance between the two neighboring activating cations, as well as the photoluminescence efficiency of RE^{3+} in doped systems [66]. Fig. 6 shows the relationship between the photoluminescence intensity and the Pr^{3+} concentration (mol%).

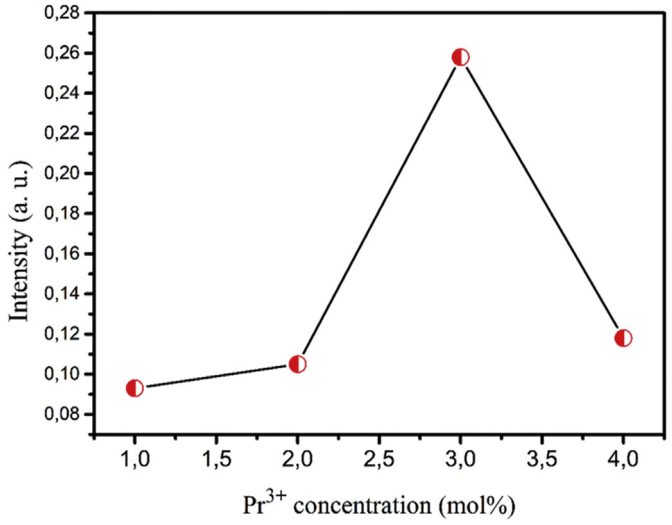

Fig. 6. Relationship between photoluminescence intensity and Pr^{3+}concentration (mol %).

A decrease in the emission intensity shows that the energy migrates among Pr^{3+} cations in different sites in the lattice, resulting in concentration quenching. Thus, optimum Pr^{3+}concentration is found to be 3 mol% (Xc = 0.03). Concentration quenching occurs by the non-radioactive migration of energy among Pr^{3+} cations. The migration of non-radioactive energy can take place from two distinct mechanisms: i. e (i) Forster resonance energy transfer (multipole-multipole interaction) and (ii) Dexter mechanism (exchange interaction) [67].

The critical energy transfer distance (Rc) for Y_2MoO_6:Pr^{3+} was estimated by equation (3) suggested by Blasse [68] from the structure parameters, namely the unit cell volume (V), the number of units of the molecular formula per unit cell (Z) and the quenching concentration (Xc).

$$Rc \cong 2\left(\frac{3V}{4Xc\pi Z}\right)^{1/3} \quad (3)$$

For the Y_2MoO_6: 3%Pr^{3+} system, the following values were considered: Z = 8, V = 916.10 $Å^3$ and Xc = 0.03, the calculated Rc was 19.40 Å. Normally, the exchange interaction is preferably in an energy transfer process when the Rc value is between 5 and 10 Å [69]. In case of values higher than 10 Å, there is no indication of exchange interaction in this mechanism. Consequently, other multipolar electrical interactions are responsible for the quenching effect between two more activating ions (Pr^{3+}).

$[MoO_4]^{2-}$ clusters act as sensitizers for Pr^{3+}. They are able to

absorb the excitation energy ($\lambda_{exc} = 350$ nm) more efficiently, as can be seen in the UV–Vis absorption spectrum result indicated in Fig. 4. This result is in agreement with other works reported in literature [70]. A strong absorption in the ultraviolet occurs due to the charge transfer in $[MoO_4]^{2-}$groups, and part of this energy is transferred to Pr^{3+} ions. To clearly demonstrate the luminescence process, a schematic diagram is shown in Fig. 7.

According to Brenier and Kityk [71], the main reason for the low cross-relaxation in the photoluminescent processes is the specific influence of 2p-type potential ligands (oxygen) in the transition moments of dipoles, determining the probabilities of particular level occupations. Another possibility of level occupation is connected with the multiphonic decay for $^1D_2$ of Pr^{3+} level. According to the authors, it was evaluated that the multiphonic contribution to the $^1D_2$ emission corresponds to about 12%, being, therefore, twice as large as the particular processes of cross relaxation.

According to the spectra distribution, the chromaticity coordinates (Xc, Yc) were calculated. Fig. 5(c) represents the CIE diagram, identifying all samples emitted in the white region. It was observed that as the Pr^{3+} concentration increases, there is a tendency of yellow emission. The correlative color temperature (CCT) and the color rendering index (CRI) were calculated. All samples presented CRI levels higher than 90%, indicating that samples exhibited behavior close to natural light. The National Institute of Standard and Technology (NIST) evaluated the quality of colors from CRI measurements, and that closer to 100% presents a degree of precision in the reproduction of colors of a certain object. Table 3 shows the values of chromaticity coordinates, CCT, CRI and the color of the light emitted.

Table 3
CIE coordinate values, color temperature and color rendering index.

Samples	(Xc)	(Yc)	CCT (K)	CRI (%)	Region
Y_2MoO_6	0.34	0.32	5073	91	White
Y_2MoO_6: 1% Pr	0.36	0.34	4373	95	
Y_2MoO_6: 2% Pr	0.39	0.35	3503	94	
Y_2MoO_6: 3% Pr	0.39	0.38	3774	94	
Y_2MoO_6: 4% Pr	0.39	0.41	3988	94	

3.4. Decay profiles of Y_2MoO_6: x%Pr^{3+}

Decay was recorded for $^1D_2 \rightarrow {}^3H_4$ transition of Pr^{3+} at 612 nm emission. The decay curves of all Y_2MoO_6: x%Pr^{3+} samples exhibited bi-exponential decay as shown in Fig. 8 and were fitted into exponential equation (4). The average lifetime for the bi-exponential decay was calculated from the following formula (5). The calculated decay parameters are listed in Table 4.

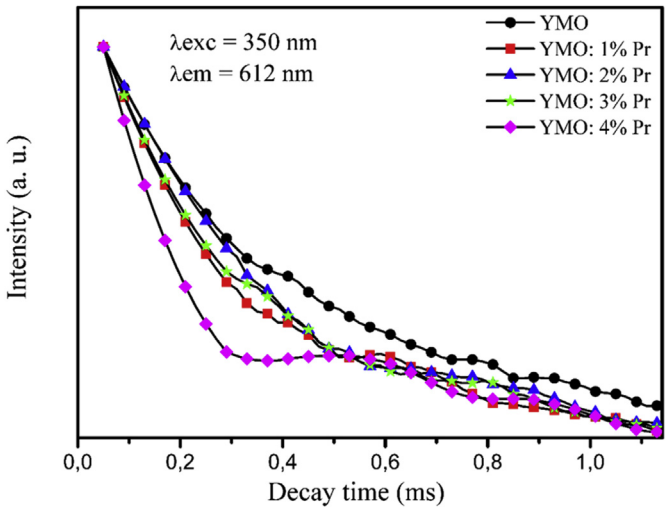

Fig. 8. Decay Curves of Y_2MoO_6: x%Pr^{3+}.

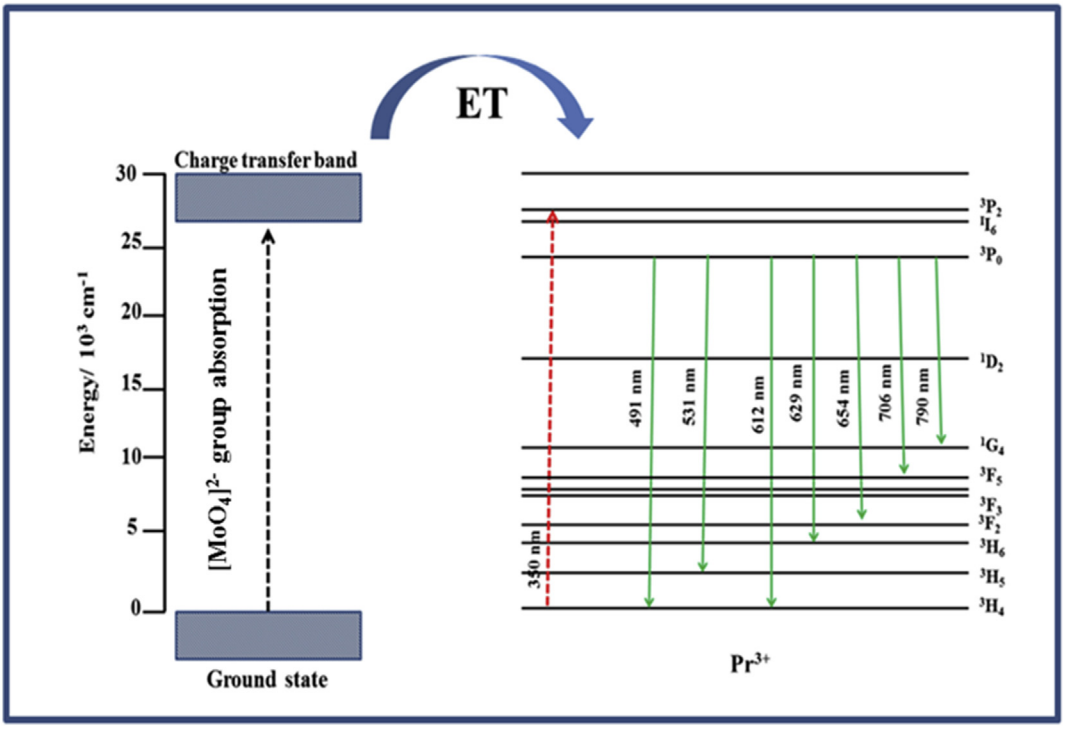

Fig. 7. Schematic representation of the energy transfer between $[MoO_4]^{2-}$ cluster and Pr^{3+} ion.

Table 4
Comparison of emission lifetimes of Y_2MoO_6: x%Pr^{3+}.

Samples	λ_{exc} (nm)	λ_{em} (nm)	A_1	τ_1 (ms)	A_2	τ_2 (ms)	τ (ms)
Y_2MoO_6	350	612	35.53	0.14	82.56	0.50	0.64
Y_2MoO_6: 1% Pr	350	612	88.88	0.53	61.64	0.07	0.6
Y_2MoO_6: 2% Pr	350	612	90.84	0.32	90.84	0.32	0.64
Y_2MoO_6: 3% Pr	350	612	78.20	0.48	33.41	0.06	0.55
Y_2MoO_6: 4% Pr	350	612	55.44	0.26	20.30	0.06	0.32

$$I = A1exp^{\frac{(-\tau)}{(\tau 1)}} + A2exp^{\frac{(-\tau)}{(\tau 2)}} \quad (4)$$

Where I is the emission intensity at any time "τ" after switching off the excitation illumination, A_1, A_2 are constant. τ_1, τ_2 are the bi-exponential component of the decay time. The average lifetime for 612 nm emission can be determined by the following formula (5):

$$\tau = \frac{(A1.\tau 1^2) + (A2.\tau 2^2)}{(A1.\tau 1 + A2.\tau 2)} \quad (5)$$

And the energy transfer efficiency from host to Pr^{3+} can be calculated according to equation (6) [72]:

$$n = \left(1 - \frac{\tau}{\tau_0}\right) x100\% \quad (6)$$

Where τ and τ_0 are the corresponding emission lifetime of the donor in the presence and absence of acceptor (Pr^{3+}) for the same donor concentration, respectively. The energy transfer efficiency from host to Pr^{3+} in Y_2MoO_6 is 50% for the Y_2MoO_6: 3%Pr^{3+} sample.

3.5. Scanning electron microscopy of Y_2MoO_6: x% Pr^{3+} particles

Fig. 9 shows the high resolution SEM image of Y_2MoO_6: x% Pr^{3+} particles. The microscopic characterization allowed the comprehension of the process of particle morphology formation as a function of the route synthesis and thermal treatment used in particles. In the crystallization processes, the solute is transferred from liquid to a solid phase due to the difference in the chemical potential between phases. Crystallization is described by combining the following mechanisms: nucleation, crystal growth and side effects such as agglomeration [73]. The fit among these mechanisms defines the particle size distribution until the end of the crystal growth. Particle agglomerates of nanometric sizes are observed in the image. The size of these particles depends on the nucleation rate of the precipitate and its dependence over time

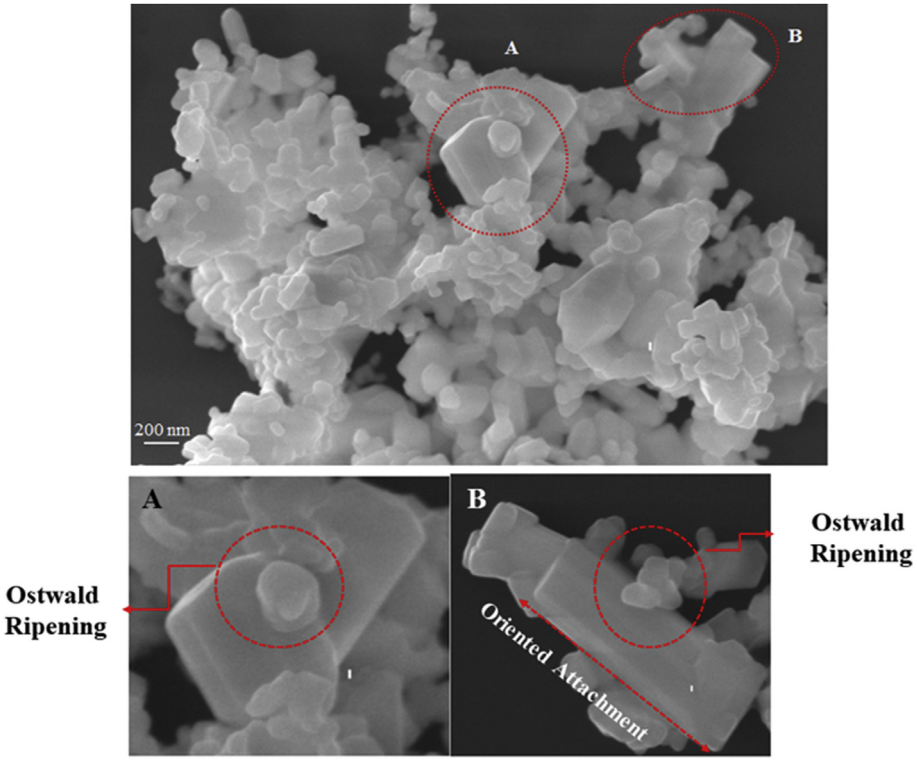

Fig. 9. SEM image of Y_2MoO_6: 1% Pr^{3+}particles.

[74]. The nucleation step is predominant at the beginning of the process when the chemical potential difference between solution and the solid phase is typically high. Smaller particles exhibit great thermodynamic instability due to the large surface area/volume ratio. A spontaneous process shown in Fig. 9(A) shows that smaller particles adhere to the surface of larger particles, which phenomenon is known as Ostwald Ripening (**OR**) and is thermodynamically favored due to the decrease of the surface energy of particles [75]. The **OR** process occurs naturally since larger particles are energetically favored by smaller ones, resulting in coalescence.

The presence of some particles with regular sides and with cube-type morphology was verified. It was observed that these crystals are made up of a series of smaller particles and have a preferred orientation, as can be seen in Fig. 9(B). This type of growth mechanism well reported in literature [76] is known as Oriented Attachment. This process consists of an aligned growth of particles in a certain crystallographic direction, and consequently coalescence of neighboring particles, eliminating the common

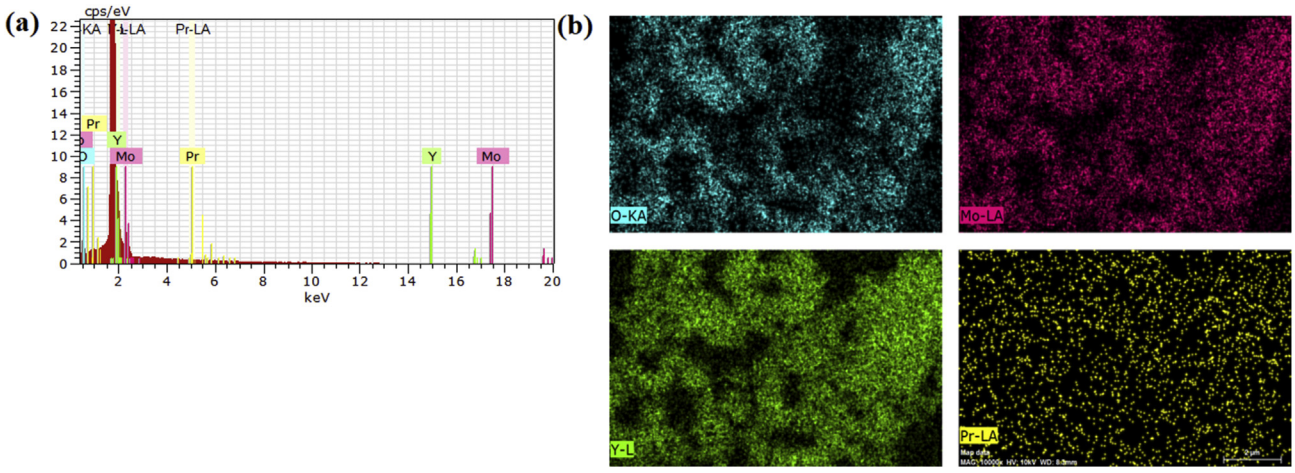

Fig. 10. EDS spectrum and mapping of atoms of Y_2MoO_6: 3%Pr^{3+} phosphor.

interface among particles, while other particles have a disoriented growth. This preferential growth can be justified by the reduction of the surface energy in a given plane that is adjusted by a specific arrangement and coordination of atoms [77,78]. Thus, it is possible to verify that some particles presented anisotropic behavior.

Fig. 10 shows the EDS spectrum and the mapping of the distribution of atoms of Y_2MoO_6: 3%Pr^{3+} phosphor to prove the chemical composition of the material produced as well as to verify the homogeneity of Zn, Mo, O and Pr throughout the sample.

4. Conclusions

Y_2MoO_6 and Y_2MoO_6:x%Pr^{3+}particles were successfully obtained by the co-precipitation method. It was shown that in Y_2MoO_6-based phosphor, the energy transfer from $[MoO_4]^{2-}$ anion to Pr^{3+} leads to visible emission. Samples showed emission in white, with chromaticity coordinate values very close to the ideal white (0.33, 0.33). The color rendering index presented levels exceeding 90%. The energy levels of Pr^{3+} ions in each site were identified from the emission spectra and their lifetime was discussed. It could be concluded that Y_2MoO_6: Pr^{3+}phosphor is a potential candidate as phosphor for application in white LEDs.

Acknowledgments

The authors thank the financial support from the following Brazilian research financing institutions: CNPq, CAPES and Programa de Pós-Graduação em Ciência e Engenharia de Materiais (PPGCEM-UFRN) for their financial support.

Appendix A. Supplementary data

Supplementary data related to this article can be found at https://doi.org/10.1016/j.jallcom.2018.07.339.

References

[1] J. Zhang, G.M. Cai, G.X. Zhang, Z.P. Jin, Insight into crystal structure and Eu/Tb doped luminescence property of a new phosphate, J. Alloys Compd. 762 (2018) 444–455.
[2] S. Redon, G. Eucat, M. Ipuy, E. Jeanneau, Y. Bretonnière, Tuning the solid-state emission of small push-pull dipolar dyes to the far-red through variation of the electron-acceptor group, Dyes Pigments 156 (2018) 116–132.
[3] B. Deng, Z. Wu, C.S. Zhou, H. Liu, A multicolor phosphor of self- and Eu3+ -activated La3Ga4TiO14, Mater. Lett. 222 (2018) 1–4.
[4] G.M. Cai, N. Yang, H.X. Liu, J.Y. Si, Y.Q. Zhang, Single-phased and color tunable $LiSrBO_3$:Dy^{3+}, Tm^{3+}, Eu^{3+} phosphors for white-light-emitting application, J. Lumin. 187 (2017) 211–220.
[5] Z. Li, H. Ma, N. Li, Y. Du, Q. Shao, New phosphors of β-BaB_2O_4:RE^{3+} (RE^{3+} = Eu^{3+}, Tb^{3+}), J. Alloys Compd. 747 (2018) 340–347.
[6] J.S. Zhong, H.B. Gao, Y.J. Yuan, L.F. Chen, D.Q. Chen, Z.G. Ji, Eu^{3+}-doped double perovskite-based phosphor-in-glass color converter for high-power warm w-LEDs, J. Alloys Compd. 735 (2018) 2303–2310.
[7] J. Zhong, D. Chen, X. Chen, K. Wang, X. Li, Y. Zhu, Z. Ji, Efficient rare-earth free red-emitting Ca_2YSbO_6:Mn^{4+}, M (M = Li^+, Na^+, K^+, Mg^{2+}) phosphors for white light-emitting diodes, Dalton Trans. 47 (2018) 6528–6537.
[8] J. Liang, P. Du, H. Guo, L. Sun, B. Li, X. Huang, High-efficiency and thermal-stable $Ca_3La(GaO)_3(BO_3)_4$:Eu^{3+} red phosphors excited by near-UV light for white LEDs, Dyes Pigments 157 (2018) 40–46.
[9] Q.Q. Zhu, X. Xu, L. Wang, Z.F. Tian, Y.Z. Xu, A robust red emitting phosphor-in-glass (PIG) for use in white lighting sources pumped by blue laser diodes, J. Alloys Compd. 702 (2017) 193–198.
[10] R. Xiang, X.J. Liang, Q. Xi, Z.F. Yuan, C. Chen, W.D. Xiang, A chromaticity-tunable white LED by screen-printing red phosphor coating on PIG plates, Ceram. Int. 42 (2016) 19285–19291.
[11] Z. Yahiaoui, M.A. Hassairi, M. Dammak, E. Cavalli, Tunable luminescence and near white-light emission of YPO_4:Eu^{3+}, Tb^{3+},Tm^{3+} phosphors, J. Alloys Compd. 763 (2018) 56–61.
[12] M. Mungraa, F. Steudelb, B. Ahrensa, S. Schweizera, Tm/Tb/Eu triple-doped lithium aluminoborate glass for white light generation, J. Lumin. 192 (2017) 71–76.
[13] V. Naresh, K. Gupta, C.P. Reddy, B.S. Hamd, Energy transfer and colour tunability in UV light induced Tm^{3+}/Tb^{3+}/Eu^{3+}: ZnB glasses generating white light emission, Spectrochim. Acta, Part A 175 (2017) 43–50.
[14] Z. Yang, C. Ji, G. Zhang, G. Han, H. Wang, H. Bu, D. Xu, J. Sun, Crystal structure and luminescence property of a single-phase white light emission phosphor $Sr_3YNa(PO_4)_3F$:Dy^{3+}, J. Mater. Sci. Mater. Electron. 29 (2018) 12632–12638.
[15] T. Grzyb, A. Szczeszak, J. Rozowska, J. Legendziewicz, S. Lis, Tunable luminescence of Sr_2CeO_4:M^{2+} (M = Ca, Mg, Ba, Zn) and Sr_2CeO_4:Ln^{3+} (Ln = Eu, Dy, Tm) nanophosphors, J. Phys. Chem. C 116 (2018) 3219–3226.
[16] Z. Yahiaoui, M.A. Hassairi, M. Dammak, E. Cavalli, Tunable luminescence and near white-light emission of YPO_4:Eu^{3+}, Tb^{3+}, Tm^{3+} phosphors, J. Alloys Compd. 763 (2018) 56–61.
[17] K. Mondal, D.K. Singh, J. Manam, Spectroscopic behavior, thermal stability and temperature sensitivity of Ca_2SiO_4: Eu^{3+} red emitting phosphor for solid state lighting application, J. Alloys Compd. 761 (2018) 41–51.
[18] M. Shang, C. Li, J. Lin, How to produce white light in a single-phase host, Chem. Soc. Rev. 43 (2014) 1372.
[19] L. Xing, W. Yang, J. Lin, M. Huang, Y. Xue, Enhanced and stable upconverted white-light emission in Ho^{3+}/Yb^{3+}/Tm^{3+}-doped $LiNbO_3$Single crystal via Mg^{2+} ion doping, Sci. Rep. 7 (2017) 14725.
[20] L.X. Lovisa, J. Andres, L. Gracia, M.S. Li, C.A. Paskocimas, M.R.D. Bomio, V.D. Araujo, E. Longo, F.V. Motta, Photoluminescent properties of ZrO_2: Tm^{3+}, Tb^{3+}, Eu^{3+}powders—a combined experimental and theoretical study, J. Alloys Compd. 695 (2017) 3094–3103.
[21] D. Böhnisch, F. Baur, T. Jüstel, Photoluminescence and energy transfer behavior of narrow band red light emitting $Li_3Ba_2Tb_3(MoO_4)_8$: Eu^{3+}, Dalton Trans. 47 (2018) 1520–1529.
[22] F. Ruan, D. Deng, M. Wu, C. Wu, S. Xu, Tunable single-host full-color-emitting $Ca_9Zn_{1.5}(PO_4)_7$: Eu, Tb phosphor via Eu^{2+}/Eu^{3+} dual-emitting, J. Lumin. 198 (2018) 1–9.
[23] J. Zhang, N. Wang, Y. Guo, M. Cai, Y. Tian, F. Huang, S. Xu, Tm^{3+}-doped lead silicate glass sensitized by Er^{3+} for efficient ~ 2μm mid-infrared laser material, Spectrochim. Acta, Part A 199 (2018) 65–70.
[24] R. Praveena, V.S. Sameera, P. Babu, Ch Basavapoornima, C.K. Jayasankar,

Photoluminescence properties of Ho^{3+}/Tm^{3+}-doped YAGG nanocrystalline powders, Opt. Mater. 72 (2017) 666–672.
[25] Y. Tai, X. Du, X. Li, B. Pan, G. Yuan, H. Wang, Efficient near–infrared down conversion by two–step energy transfer from Pr^{3+} to Yb^{3+} in transparent nanostructured glass ceramics, J. Photochem. Photobiol., A 360 (2018) 64–70.
[26] X. Wu, W. Bai, O. Hai, Q. Ren, F. Lin, Y. Jiao, Structure, luminescence properties and energy transfer of Dy^{3+} and Eu^{3+} codoped $KBa(VO_4)$ phosphor, J. Solid State Chem. 265 (2018) 109–116.
[27] X. Tan, Y. Wang, M. Zhang, Solvothermal synthesis, luminescence and energy transfer of Dy^{3+} and Sm^{3+} doped $NaLa(WO_4)_2$ nanocubes, J. Photochem. Photobiol., A 353 (2018) 65–70.
[28] C.R.R. Almeida, L.X. Lovisa, A.A.G. Santiago, M.S. Li, E. Longo, C.A. Paskocimas, F.V. Motta, M.R.D. Bomio, One-step synthesis of CaMoO4: Eu3+ nanospheres by ultrasonic spray pyrolysis, J. Mater. Sci. Mater. Electron. 22 (2017) 16867–16879.
[29] S. Li, Q. Meng, S. Lü, W. Sun, Study on optical temperature sensing properties of Tb^{3+}, Eu^{3+} co-doped $CaMoO_4$ phosphor, J. Lumin. 200 (2018) 103–110.
[30] S.K. Jaganathana, A.J. Peterd, Synthesis and luminescence properties of $CaGd_2(MoO_4)_4$:Ln^{3+} (Ln = Eu^{3+}, Tb^{3+}, Dy^{3+} and Sm^{3+}) phosphors, J. Lumin. 199 (2018) 53–59.
[31] Y.P. Gao, K.J. Huang, C.X.Z. hang, S.S. Song, High-performance symmetric supercapacitor based on flower-like zinc molybdate, J. Alloys Compd. 731 (2018) 1151–1158.
[32] A. Xie, Z. Yu, H. Zhang, R. Guo, Luminescent enhancement mechanism of Bi^{3+} Co-doped CaMoO4:Eu^{3+} investigated by TEM, J. Alloys Compd. 708 (2017) 476–483.
[33] H. Dejian, P. Xixiang, L. Jinyan, Z. Weijie, Y. Xinyu, Structure and luminescence properties of Sm^{3+}doped Y_2MoO_6phosphor under near ultraviolet light excitation, J. Rare Earths 35 (2017) 335.
[34] C. Cui C, et al., Copper(I)-Catalyzed cascade dearomatization of 2-substituted tryptophols with arylidonium salts, Mater. Lett. 61 (2017) 4525–4527.
[35] M. Pawlikowska, M. Piatkowska, E. Tomaszewic, 1 Synthesis and thermal stability of rare-earths molybdates and tungstates with fluorite- and scheelite-type structure, J. Therm. Anal. Calorim. 130 (2017) 69–76.
[36] K. Thomas, D. Alexander, S. Sisira, P.R. Biju, N.V. Unnikrishnan, M.A. Ittyachen, C. Joseph, NUV/blue LED excitable intense green emitting terbium doped lanthanum molybdate nanophosphors for white LED applications, J. Mater. Sci. Mater. Electron. 28 (2017), 7702–17709.
[37] D. Errandonea, F.J. Manjon, Pressure effects on the structural and electronic properties of ABX_4 scintillating crystals, Prog. Mater. Sci. 53 (2008) 711–773.
[38] J.A. Alonso, F. Rivillas, M.J. Martínez-Lope, V. Pomjakushin, Preparation and structural study from neutron diffraction data of R_2MoO_6 (R = Dy, Ho, Er, Tm, Yb, Y), J. Solid State Chem. 177 (2004) 2470.
[39] T. Schleid, S. Strobel, P.K. Dorhout, P. Nockemann, K. Binnemans, I. Hartenbach, YF[MoO_4] and YCl[MoO_4]: two halide derivatives of yttrium *ortho*-oxomolybdate: syntheses, structures, and luminescence properties, Inorg. Chem. 47 (2008) 3728–3735.
[40] M. Wang, et al., Charge transfer bands of Mo–O and photoluminescence properties of micro-material Y_2MoO_6:Eu^{3+}red phosphor, J. Alloys Compd. 585 (2014) 138–145.
[41] L. Sójka, Z. Tang, D. Furniss, H. Sakr, A. Oladeji, E. Bereś-Pawlik, H. Dantanarayana, A.B. Seddon, T.M. Benson, S. Sujecki, Broadband, mid-infrared emission from Pr^{3+} doped GeAsGaSe chalcogenide fiber, optically clad, Opt. Mater. 36 (2014) 1076–1082.
[42] G.A.S. Flizikowski, V.S. Zanuto, A. Novatski, L.A.O. Nunes, L.C. Malacarne, M.L. Baesso, N.G.C. Astrath, Upconversion luminescence and hypersensitive transitions of Pr^{3+}–doped calcium aluminosilicate glasses, J. Lumin. 202 (2018) 27–31.
[43] J.Q. Qi, J.X. Chang, R.Q. Zhang, Q.Q. Zhang, B.D. Liu, J. Chen, X.M. Han, Processing, point defects and photoluminescence of Pr-$CaTiO_3$ phosphors, Ceram. Int. 44 (2018) 14342–14347.
[44] O.A. Morozov, A.K. Naumov, A.V. Lovchev, E. Yu, Tselishcheva up-conversion luminescence of LaF_3:Pr^{3+} crystal, J. Phys. Conf. Ser. 560 (2014), 012012.
[45] Y. Chen, J. Wang, M. Zhanga, Q. Zenga, Light conversion material: $LiBaPO_4$: Eu^{2+}, Pr^{3+}, suitable for solar cell, RSC Adv. 7 (2017) 21221–21225.
[46] H. Rietveld, A profile refinement method for nuclear and magnetic structures, J. Appl. Crystallogr. 2 (1969) 65–71.
[47] B. Toby, EXPGUI, a graphical user interface for GSAS, J. Appl. Crystallogr. 34 (2001) 210–213.
[48] K. Momma, F. Izumi, VESTA 3 for three-dimensional visualization of crystal, volumetric and morphology data, J. Appl. Crystallogr. 44 (2011) 1272–1276.
[49] B. Han, J. Zhang, Z. Wang, Y. Liu, H. Shi, Investigation on the concentration quenching and energy transfer of red-light-emitting phosphor Y_2MoO_6: Eu, J. Lumin. 149 (2014) 150–154.
[50] J.M. Zhang, Y. Zhang, K.W. Xu, V. Ji, General compliance transformation relation and applications for anisotropic hexagonal metals, Solid State Commun. 139 (2006) 87–91.
[51] D. Hou, X. Pan, J. Li, W. Zhou, X. Ye, Structure and luminescence properties of Sm^{3+} doped Y_2MoO_6 phosphor under near ultraviolet light excitation, J. Rare Earths 35 (2017) 335.
[52] M. Pang, X. Liu, Luminescence properties of R_2MoO_6:Eu^{3+} (R = Gd, Y, La) phosphors prepared by Pechini sol-gel process, J. Mater. Res. 20 (2005) 2676–2681.
[53] P. Kubelka, New contributions to the optics of intensely light-scattering materials Part I, J. Opt. Soc. Am. B 38 (1984) 448–457.
[54] H. Deng, Photoluminescence properties of a new orange–red emitting Sm3+-doped $Y_2Mo_4O_{15}$ phosphor, J. Solid State Chem. 228 (2015) 110–116.
[55] A. Vyas, R.A. Talewar, A. Muley, C.P. Joshi, S.V. Moharil, NIR emitting phosphors based on sensitization by molybdate anion, J. Lumin. 194 (2018) 656–660.
[56] J.C. Sczancoski, L.S. Cavalcante, N.L. Marana, R.O. Da Silva, R.L. Tranquilin, M.R. Joya, P.S. Pizani, J.A. Varela, J.R. Sambrano, M. Siu Li, E. Longo, J. Andrés, Electronic structure and optical properties of $BaMoO_4$ powders, Curr. Appl. Phys. 10 (2010) 614–624.
[57] J. Milanez, A.T. de Figueiredo, S. de Lazaro, V.M. Longo, R. Erlo, V.R. Mastelaro, R.W.A. Franco, E. Longo, J.A. Varela, The role of oxygen vacancy in the photoluminescence property at room temperature of the $CaTiO_3$, J. Appl. Phys. 106 (2009), 043526.
[58] J.S. Kim, H.L. Park, C.M. Chon, H.S. Moon, T.W. Kim, The origin of emission color of reduced and oxidized $ZnGa_2O_4$ phosphors, Solid State Commun. 129 (2004) 163.
[59] H.F. Brito, J. Holsa, H. Jungner, T. Lamanen, M.H. Lastusaari, M. Malkanmaki, L.C.V. Rodriguess, Opt. Mater. Express 2 (2012) 287.
[60] S. Yin, D. Chen, W. Tang, Combustion synthesis and luminescent properties of $CaTiO_3$: Pr, Al persistent phosphors, J. Alloys Compd. 441 (2007) 327.
[61] B.M. Mothudi, O.M. Ntwaeaborwa, Shreyas S. Pitale, H.C. Swart, Luminescent properties of $Ca_{0.97}Al_2O_4$:Eu-0.01(2+),DY0.023+ phosphors prepared by combustion method at different initiating temperatures, J. Alloys Compd. 508 (2010) 262.
[62] B.M. Mothudi, O.M. Ntwaeaborwa, J.R. Botha, H.C. Swart, Photoluminescence and phosphorescence properties of MAl2O4: Eu^{2+}, Dy^{3+} (M= Ca, Ba, Sr) phosphors prepared at an initiating combustion temperature of 500° C, Physica B 404 (2009) 4440.
[63] Y. Li, Y. Wang, X. Xu, G. Yu, N. Wang, Electronic structures and Pr^{3+} photoluminescence characteristics in fresnoite, Sr- fresnoite, and Ge-Fresnoite, J. Am. Ceram. Soc. 94 (2011) 496–500.
[64] Y. Huang, L. Luo, J. Wang, Q. Zuo, Y. Yao, W. Li, The down-conversion photoluminescence properties of $Na_{0.5}Bi_{0.5}TiO_3$: Yb^{3+}/Pr^{3+} ceramics, J. Appl. Phys. 118 (2015), 044101.
[65] M. Inokuti, F. Hirayama, Influence of energy transfer by the exchange mechanism on donor luminescence, J. Chem. Phys. 4 (1965) 1978.
[66] F. Wang, X.G. Liu, Recent advances in the chemistry of lanthanide-doped upconversion nanocrystals, Chem. Soc. Rev. 38 (2009) 976.
[67] P. Jena, S.K. Gupta, V. Natarajan, M. Sahu, N. Satyanarayana, M. Venkateswarlu, Structural characterization and photoluminescence properties of solegel derived nanocrystalline $BaMoO_4$:Dy^{3+}, J. Lumin. 158 (2015) 203–210.
[68] G. Blasse, Energy transfer in oxidic phosphors, Phys. Lett. A 28 (1968) 444.
[69] F. Kang, Y. Zhang, M. Peng, Controlling the energy transfer via multi luminescent centers to achieve white light/tunable emissions in a single-phased X2-Type Y_2SiO_5: Eu^{3+}, Bi^{3+}phosphor for ultraviolet converted LEDs, Inorg. Chem. 54 (2015) 1462.
[70] H.R. Shih, L.G. Teoh, H.Z. Lin, Y.J. Chen Chang, Preparation and photoluminescence properties of Pr^{3+} ion-doped Ca_2LaTaO_6 phosphors, J. Electron. Mater. 43 (2014) 1091–1096.
[71] A. Brenier, I.V. Kityk, Spectroscopic properties of Pr^{3+}-doped $Ca_4GdO(BO_3)_3$(GdCOB), J. Appl. Phys. 90 (2001) 232.
[72] P. Boutinaud, L. Sarakha, E. Cavalli, M. Bettinelli, P. Dorenbos, R. Mahiou, About red afterglow in Pr^{3+} doped titanate perovskites, J. Phys. D Appl. Phys. 42 (2009) 045106–045112.
[73] M. Janulevicius, P. Marmokas, M. Misevicius, J. Grigorjevaite, L. Mikoliunaite, S. Sakirzanovas, A. Katelnikovas, Luminescence and luminescence quenching of highly efficient $Y_2Mo_4O_{15}$:Eu^{3+} phosphors and ceramics, Sci. Rep. 6 (2016) 26098.
[74] T. Vetter, M. Iggland, D.R. Ochsenbein, F.S. Hanseler, M. Mazzotti, Modeling nucleation, growth, and Ostwald ripening in crystallization processes: a Comparison between population balance and kinetic rate equation, Cryst. Growth Des. 13 (2013) 4890–4905.
[75] C. Lindenberg, M. Mazzotti, Continuous precipitation of L-asparagine monohydrate in a micromixer: estimation of nucleation and growth kinetics, AIChE J. 57 (2011) 942–950.
[76] G.M. Gurgel, L.X. Lovisa, L.M. Pereira, F.V. Motta, M. Siu Li, E. Longo, C.A. Paskocimas, M.R.D. Bomio, Photoluminescence properties of (Eu, Tb, Tm) co-doped $PbMoO_4$ obtained by sonochemical synthesis, J. Alloys Compd. 700 (2017) 130.
[77] S. Jia, H. Zheng, H. Sang, W. Zhang, H. Zhang, L. Liao, J. Wang, Self-assembly of $KxWO_3$ nanowires into nanosheets by an oriented attachment mechanism, ACS Appl. Mater. Interfaces 5 (2013) 10346.
[78] A.F. Gouveia, M.M. Ferrer, J.R. Sambrano, J. Andrés, E. Longo, Modeling the atomic-scale structure, stability, and morphological transformations in the tetragonal phase of $LaVO_4$, Chem. Phys. Lett. 660 (2016) 87.